Evaluation of Sputtered Nickel Oxide, Cobalt Oxide and Nickel-Cobalt Oxide on n-type Silicon Photoanodes for Solar-Driven O2(g) Evolution from Water

Evaluation of Sputtered Nickel Oxide, Cobalt Oxide and Nickel-Cobalt Oxide on n-type Silicon Photoanodes for Solar-Driven O$_2$(g) Evolution from Water

Fan Yang, Xinghao Zhou, Noah T. Plymale, Ke Sun, and Nathan S. Lewis*

[1]Division of Chemistry and Chemical Engineering, 127-72, California Institute of Technology, Pasadena, CA 91125, USA

*Correspondence to: nslewis@caltech.edu

ABSTRACT

Thin films of Nickel oxide (NiO$_x$), Cobalt oxide (CoO$_x$) and Nickel-cobalt oxide (NiCoO$_x$) were sputtered onto n-Si(111) surfaces to produce a series of integrated, protected Si photoanodes that did not require deposition of a separate heterogeneous electrocatalyst for water oxidation. The p-type transparent conductive oxides (p-TCOs) acted as multi-functional transparent, antireflective, electrically conductive, chemically stable coatings that also were active electrocatalysts for the oxidation of water to O$_2$(g). Relative to the formal potential for water oxidation to O$_2$, $E^{o'}$(O$_2$/H$_2$O), under simulated Air Mass (AM)1.5 illumination the p-TCO-coated n-Si(111) photoanodes produced mutually similar open-circuit potentials of -270 ± 20 mV, but different photocurrent densities at $E^{o'}$(O$_2$/H$_2$O), of 28 ± 0.3 mA cm^{-2} for NiO$_x$, 18 ± 0.3 mA cm^{-2} for CoO$_x$ and 24 ± 0.5 mA cm^{-2} for NiCoO$_x$. The p-TCOs all provided protection from oxide growth for extended time periods, and produced stable photocurrent densities from n-Si in 1.0 M KOH(aq) (ACS grade) under potential control at $E^{o'}$(O$_2$/H$_2$O) for >400 h of continuous operation under 100 mW cm^{-2} of simulated AM1.5 illumination.

INTRODUCTION

Silicon, with a band-gap of 1.1 eV, has been widely explored for use in photoelectrochemical water-splitting device as either a photocathode or photoanode. However, Si rapidly corrodes and passivates oxidatively when in contact with aqueous alkaline electrolytes.[1] The kinetically slow four-electron-transfer oxygen-evolution reaction (OER): $4OH^- \rightarrow 2H_2O + O_2 + 4e^-$ (in alkaline media) has a high overpotential and requires electrocatalysts to proceed efficiently.[2] Operationally useful overlayers on Si photoelectrodes thus would be electrocatalytic for the oxidation of H_2O to $O_2(g)$, conformal on the Si surface even on nanostructured electrodes, and would facilitate conduction of photogenerated charge carriers across the solid/liquid interface.

OER electrocatalysts comprised of precious metals, such as IrO_2 and RuO_2 [3-5] exhibit high activity and high relative stability in aqueous acidic or alkaline media. Electrocatalysts formed using more abundant metals, such as transition-metal oxides derived from NiO_x, CoO_x and $NiCoO_x$, have recently attracted considerable attention. n-Silicon photoanodes have been protected using highly transparent NiO_x films formed by sol-gel processes,[6] e-beam evaporation,[7] drop-casting[8] or reactive sputtering.[9] Fe incorporation from the KOH solution into NiO_x forms a nickel–iron oxyhydroxide that enhances the OER activity of such films.[10] In alkaline solution, NiO_x coverts to structurally porous $Ni(OH)_2/NiOOH$,[11-13] which when used for protection from corrosion or passivation will affect the long-term integrity of photoelectrodes. CoO_x has also been used as an OER catalyst as well as to produce interfacial layers to effect band-edge engineering on Si photoanodes for water oxidation. CoO_x nanoparticles have been formed using cyclic voltammetry on glassy carbon substrates,[14] whereas CoO_x films have

been formed by electrodeposition on rotating disk electrodes.[15] Moreover, CoO_x has been deposited by plasma-enhanced atomic-layer deposition (ALD) on a nanostructured p^+n-Si electode,[16] and CoO_x thin layers have been deposited by ALD as an interfacial layer between Si and NiO_x.[17] CoO_x has a smaller band-gap, and is a less active electrocatalyst for water oxidation, than NiO_x. Binary metal oxides, such as $NiCoO_x$, have also been investigated as p-type transparent conductive oxides.[18] Amorphous nanoporous Ni-Co binary oxide layers that act as an efficient OER catalyst have been fabricated by electrochemical deposition.[19] P-type $NiCo_2O_x$ has been sputtered as a hole conducting protection layer onto n-Si and n-InP photoanodes, with a 2 nm Ni-Fe film serving as the OER catalyst.[20] A co-sputtered $Co/NiCoO_x$ on n^+pp^+ Si tandem device configuration was investigated with back-side illumination in contact with 1.0 M KOH(aq).[21]

In this work, a series of earth-abundant p-TCOs consisting of NiO_x, CoO_x and $NiCoO_x$, have all been deposited onto n-Si photoanodes using reactive RF-sputtering in a mutually common fabrication process. The Co oxides are more optically absorbing than the NiO_x oxides, but Co oxides are less porous and more conductive than Ni oxyhydroxides. Using Si as a prototypical photoanode material, we have systematically evaluated and compared the activity and stability of these films at the compositional limits of pure Ni and pure Co oxides to the behavior of a mixed-metal intermediate composition oxide. We have also evaluated trends in stability, conductivity, junction interfacial energetics, and optical absorption properties when these thin film oxides were used as photoelectrode protective layers that are also intrinsically active electrocatalytically for water oxidation in alkaline media.

EXPERIMENTAL SECTION

Materials and Chemicals

All materials including sulfuric acid (H_2SO_4, J. T. Baker, ACS reagent, 95%-98%), concentrated hydrochloric acid (HCl, Sigma Aldrich, ACS Reagent 37%), hydrogen peroxide (H_2O_2, Macron Chemicals, ACS grade 30%), concentrated ammonium hydroxide (NH_4OH, Sigma Aldrich, ACS reagent 28%-30%), buffered HF Improved (Transene Company Inc.), potassium hydroxide pellets (KOH, Macron Chemicals, ACS 88%), potassium hydroxide pellets (KOH, Mallinckrodt Chemicals, FCC), potassium ferrocyanide trihydrate ($K_4Fe(CN)_6 \cdot 3H_2O$, Acros, >99%), potassium ferricyanide ($K_3Fe(CN)_6$, Fisher Chemicals, certified ACS 99.4%), and sodium sulfate (Na_2SO_4, Sigma Aldrich, ACS Reagent >99.0%), were used as received. Except where specifically stated otherwise, the KOH was ACS grade. Deionized water with a resistivity of 18.2 MΩ·cm was obtained from a Millipore water purification system.

Preparation of Substrates

Two types of 3-inch diameter Si wafers were used in this study. p^+-Si(111) wafers were boron-doped, 380 ± 25 μm thick, prime grade, and had a resistivity $\rho <$ 0.002 Ω·cm (Addison Engineering, Inc.). n-Si(111) wafers were phosphorus-doped with $\rho = 0.1–1$ Ω·cm (University Wafer, Inc.). The p-type wafers were cleaned by etching for 30 s in buffered HF, whereas the n-type wafers were cleaned using a modified RCA SC-2 procedure.[22] Before film deposition, the samples were thoroughly rinsed with deionized H_2O and dried under a flow of $N_2(g)$.

Deposition of NiO_x, CoO_x and $NiCoO_x$ with Rate Analysis

Reactive RF sputtering was performed using an AJA high-vacuum magnetron sputtering system (AJA International Inc.) with a base pressure of 8×10^{-8} Torr. Sputtering was performed under a pressure of 5 mTorr while the Ar/O_2 flow rate was maintained at 20/1 sccm. The RF power on Ni and Co targets (Kurt Lesker, 2″ diameter × 0.125″ thickness, 99.95%) was maintained at 150 W for sputtering of NiO_x and CoO_x. For sputtering of $NiCoO_x$, the Ni and Co targets were held at 115 W and 125 W, respectively, to yield a similar sputtering rate to that used for deposition of NiO_x and CoO_x. During sputtering, the stage was maintained at 300 °C.

The oxide film thickness was measured by cross-sectional scanning-electron microscopy (SEM) (Figure S1a) and stylus profilometery (Figure S1b, Bruker DektakXT, 2 μm tip, and resolution 1 nm). The sputtering rate for NiO_x, CoO_x and $NiCoO_x$ was ~ 3.6 nm min^{-1}, 3.0 nm min^{-1}, and 5.0 nm min^{-1} respectively. The film thickness was monitored using an internal quartz crystal microbalance (Inficon, SQM-160).

Scanning-electron Microscopy and Energy-dispersive X-ray spectra

Scanning-electron micrographs (SEMs) were obtained using a Nova NanoSEM 450 microscope (FEI, Hillsboro, OR, USA) with an accelerating voltage of 15 kV and a working distance of 5.0 mm. Energy-dispersive X-ray spectra (EDS) were collected at an accelerating voltage of 15 kV using a Si drift detector (Oxford Instruments, Abingdon, United Kingdom). Inca software (Oxford Instruments) was used to interpret the EDS spectra.

Atomic-force Microscopy

Atomic-force microscopy (AFM) was performed using a Bruker Dimension Icon operating in ScanAsyst mode with Bruker ScanAsyst-Air probes (silicon tip, silicon nitride cantilever, spring constant: 0.4 N/m, frequency: 50 - 90 kHz). The scan size was 1 × 1 μm and the images were analyzed using NanoScope Analyst software (version 1.40).

X-ray Diffraction Spectroscopy

X-ray Diffraction (XRD) analysis was performed using a Bruker D8 Discover system equipped with a 2-dimentional Vantec-500 detector. Cu-Ka radiation (1.54 Å) was generated at a tube voltage of 50 kV and a tube current of 1000 mA. The detected radiation was counted for 1 h. Data were analyzed using Bruker EVA software.

UV-Visible Transmission and Absorption Measurements

The optical transmittance of 75 nm-thick films of either NiO_x, CoO_x or $NiCoO_x$ on quartz substrates was measured with an integrating sphere at normal incidence (Aligent Cary 5000 UV-vis Spectrometer). The optical band-gaps were estimated using Tauc plots of $h\nu$ versus $(\alpha h\nu)^2$, where α is the absorption coefficient determined from the Beer-lambert Law. The reflectivity of 75 nm-thick films of NiO_x, CoO_x and $NiCoO_x$ on n-Si was measured at normal incidence with the integrating sphere.

Measurements of Faradaic Efficiency for Production of Oxygen

The generated $O_2(g)$ was collected and measured in a home-built eudiometer. The mass of the generated $O_2(g)$ was calculated from the volume, pressure, and temperature of the eudiometer. The n-Si photoanodes coated with p-TCOs were used as working electrodes, with a geometric area of ~1 cm^2. The reference electrode was Hg/HgO (CH Instruments, CH152) and a glass-fritted carbon rod was used as the counter

electrode. The current was maintained at 8 mA, resulting in a working electrode potential of ~ 1.8 V versus the reversible hydrogen electrode (RHE). The light intensity at the working electrode was ~ 1/3 Sun. The expected amount of oxygen generated during 24 h of continuous operation was calculated from measurement of the charge in coulombs passed during operation, taking the oxygen-evolution reaction to be a 4-electron (hole) process, and assuming 100% Faradaic efficiency for $O_2(g)$ production.

RESUTLS AND DISCUSSIONS

Figure 1 shows SEM images of 75 nm-thick NiO_x (Figure 1a), CoO_x (Figure 1b) and $NiCoO_x$ (Figure 1c) films sputtered on p^+-Si substrates. All of the sputtered films exhibited a granular surface morphology. AFM measurements indicated that the NiO_x (Figure 1d) had a surface roughness of 4.08 ± 0.03 nm; the CoO_x (Figure 1e) had a surface roughness of 4.24 ± 0.15 nm; and the $NiCoO_x$ (Figure 1f) had a surface roughness of 3.33 ± 0.07 nm. EDS data were consistent with the formation of pure NiO_x (Figure 1g) and CoO_x (Figure 1h), with the Si signal arising from the substrate. EDS indicated a Ni : Co ratio of $1:1 \pm 0.1$ for the $NiCoO_x$ film (Figure 1i).

Figure 2 shows the XRD patterns of NiO_x (red curve), CoO_x (green curve) and $NiCoO_x$ (blue curve) sputtered onto glass. All of the sputtered films were polycrystalline and single phase. Figure 2 (red curve) shows the XRD pattern of the NiO_x film, which agrees well with cubic NiO (Bunsenite, JCPDS 01-071-1179). The preferred orientation was in the <111> direction. Figure 2 (green curve) shows the XRD pattern of the CoO_x film, which agrees well with cubic Co_3O_4 (Cobalt Oxide, JCPDS 01-073-1701). The preferred orientation was in the <311> direction. Figure 2 (blue curve) shows the XRD pattern of the $NiCoO_x$ film, which agrees well with cubic $NiCoO_2$ (Cobalt Nickel Oxide,

JCPDS 00-010-0188), and the preferred orientation was in the <111> direction. The NiCoO$_x$ XRD pattern is very similar to the NiO$_x$ XRD pattern, with all the peaks slightly shifted to lower angle, in accord with the lattice expansion that accompanies incorporation of Co into NiO$_x$. Electrochemical impedance spectroscopy (EIS) indicated that the sputtered NiO$_x$, CoO$_x$ and NiCoO$_x$ films were all p-type semiconductors with a doping density in the range of 10^{19} cm^{-3} (Figure S2).

Figure 3a shows the transmittance spectra for the NiO$_x$ (red curve), CoO$_x$ (green curve) and NiCoO$_x$ (blue curve) films sputtered onto a quartz substrate, along with bare quartz (black curve) as a control. Bare quartz showed ~ 93% transmittance in the wavelength range of 300 - 1100 nm. In contrast, in the visible wavelength range of 390-700 nm, 75 nm of NiO$_x$ showed an average transmittance of ~70%, whereas 75 nm CoO$_x$ showed an average transmittance of ~30%, and 75 nm NiCoO$_x$ showed an average transmittance of ~60%. Fitting the linear portions of the Tauc plot (*hv* versus αhv^2) of NiO$_x$ yielded direct band-gap transitions at 2.6 and 3.5 eV (Figure 3b, red curve). The transmittance data for CoO$_x$ (Figure 3a, green curve) clearly showed two absorption bands, with the band at ~470 nm ascribable to the $O^{2-} \rightarrow Co^{2+}$ charge-transfer process, while the band at ~750 nm is ascribable to the $O^{2-} \rightarrow Co^{3+}$ charge-transfer process. Fitting the linear potion of the Tauc plot (hv versus ahv^2) of CoO$_x$ (Figure 3b) yielded direct band-gap transitions at 2.5 and 1.6 eV. Fitting the linear potion of the Tauc plot (hv versus $\alpha hv^{1/2}$) for NiCoO$_x$ showed a direct band-gap transition at 3.0 eV by (Figure 3b, blue curve).

Figure 4a shows 20 continuous voltammetric cycles of p$^+$-Si|NiO$_x$ (red curve), p$^+$-Si|CoO$_x$ (green curve) and p$^+$-Si|NiCoO$_x$ (blue curve) in 1.0 M KOH(aq) between 0.42

and 1.92 V versus RHE. The dark catalysis behavior typically reached steady state, without further improvement, after 20 *J-E* scans. Figure 4b (red curves) shows that as a consequence of potential cycling, the overpotential for NiO_x to produce 10 mA cm^{-2} of anodic current density ($\eta_{10 \text{ mA cm-2}}$) decreased from 500 ± 35 mV to 330 ± 5 mV, and the redox peaks became more prominent due to the formation of oxyhydroxide at the surface. Figure 4b (green curves) shows that after voltammetric scanning, $\eta_{10 \text{ mA cm-2}}$ for CoO_x increased from 390 ± 10 mV to 420 ± 10 mV, and the redox peaks of CoO_x to CoOOH were not as prominent as in the conversion of NiO_x to NiOOH. Figure 4b (blue curves) shows that $\eta_{10 \text{ mA cm-2}}$ for $NiCoO_x$ decreased after voltammetric scanning from 418 ± 43 mV to 357 ± 5 mV, and also shows moderately pronounced redox peaks, because half of the surface is NiO_x. The reported deviations in $\eta_{10 \text{ mA cm-2}}$ resulted from standard variation between samples.

Figure S3 presents a detailed comparison of the XPS data for 75 nm-thick NiO_x, CoO_x and $NiCoO_x$ films on Si before, and after, respectively, 20 voltammetric scans in 1.0 M KOH(aq). For NiO_x and $NiCoO_x$, the Ni 2p$_{3/2}$ peak exhibited an obvious transition from Ni^{2+} ($\sim$ 853.6 eV) to Ni^{3+} ($\sim$855.7 eV) (Figure S3a), in accord with expectations for the transformation of NiO to NiOOH. In contrast, no obvious difference between the spectra acquired before and after 20 scans in KOH (Figure S3b) was observed for the Co 2p$_{3/2}$ peak in either CoO_x or $NiCoO_x$, This behavior is consistent with the expected very small peak shift between CoO_x and CoOOH. The O 1s peak (Figure S3c) showed a transition from lattice oxygen ($\sim$ 529.5 eV) to surface hydroxyl groups ($\sim$531.4 eV) after voltammetric cycling, further confirming the formation of NiOOH as well as possibly indicating the formation of CoOOH.

Fe can play a critical role in enhancing the activity of NiO_x-based OER electrocatalysts.[10] From high-resolution XPS scans of the Fe 2p region, the Fe incorporation was 14.2% for NiO_x, 11.4% for CoO_x, and 8.4% for $NiCoO_x$ (Figure S4) after 20 voltammetric scans in 1.0 M KOH(aq). The intercalation of trace quantities of Fe correlated well with the enhancement of the OER catalytic activity of NiO_x (Figure 4b red curves). However, incorporation of trace Fe did not have a substantial effect on the OER catalytic activity of CoO_x, actually diminishing the activity slightly (Figure 4b, green curves). Similar amounts of Fe (8% from XPS) incorporated during 2 h of potential control at 1.58 V vs RHE have led to a ten-fold increase in the intrinsic activity of electrochemically deposited $Co(OH)_2$ films.[23] Differences in the amount of electrochemically accessible Co(Fe)OOH within sputtered CoO_x, relative to electrochemically deposited $Co(OH)_2$, could account for this discrepancy.

The OER catalytic activity of these three films was further investigated in FCC grade 1.0 M KOH(aq), which contains less Fe than the ACS grade KOH used in the experiments described above. As shown in Figure S5, based on the 20th *J-E* scans of NiO_x, CoO_x and $NiCoO_x$ in FCC grade 1.0 M KOH(aq) (Figure S5), $\eta_{10\ mA\ cm^{-2}} = 600 \pm 5$ mV for NiO_x and $\eta_{10\ mA\ cm^{-2}} = 440 \pm 8$ mV for CoO_x, whereas $NiCoO_x$ showed the lowest overpotential, $\eta_{10\ mA\ cm^{-2}} = 390 \pm 5$ mV. After 20 voltammetric scans in FCC grade 1.0 M KOH(aq), the high-resolution XPS spectra in the Fe 2p region showed almost no detectable Fe signal on NiO_x and CoO_x surfaces, and the $NiCoO_x$ surface exhibited ~ 2% Fe (Figure S6).

Figure 5a displays the reflectance spectra of 75 nm thick films of NiO_x (red curve), CoO_x (green curve) and $NiCoO_x$ (blue curve) on an n-Si substrate. A freshly etched n-Si

substrate showed an average of ~40% reflection in the visible range (Figure 5a, black curve). NiO_x, CoO_x or $NiCoO_x$ films all acted as antireflection coatings, substantially suppressing the large reflection loss from the smooth n-Si photoelectrode, while exhibiting a minimum reflection peak at ~ 600 nm. The NiO_x and $NiCoO_x$ coatings made the shiny silver-looking Si electrode appear dark blue in color, whereas the Si electrode appeared light green after being coated CoO_x. The NiO_x coating showed lower reflection in the visible range than CoO_x or $NiCoO_x$ films (Figure 5a).

The reflectance behavior is consistent with the external quantum yield (Φ_{ext}) data measured on n-Si photoanodes formed with these three different TCO coatings. Figure 5b presents Φ_{ext} measurements for 75 nm-thick NiO_x, CoO_x and $NiCoO_x$ films coated on n-Si in ACS grade 1.0 M KOH(aq) at 1.75 V versus RHE. The NiO_x coated n-Si photoelectrodes showed the highest external quantum yield, ~0.75, in the 600-800 nm wavelength range (Figure 5b, red curve). The $NiCoO_x$ displayed a slightly lower external quantum yield, with an average of ~0.65 in the 600-800 nm wavelength range (Figure 5b, blue curve). In contrast, CoO_x exhibited the lowest external quantum yield, with an average of ~0.50 in the wavelength range of 600-800 nm (Figure 5b, green curve). The n-Si photoelectrodes coated with CoO_x also exhibited two broad valleys in the spectral response, at 470 nm and 750 nm, consistent with the transmittance and reflectance measurements (Figures 3,5)

Figure 5c presents the *J-E* behavior in the presence and absence, respectively, of Air Mass (AM)1.5 illumination, for n-Si|NiO_x (red curves), n-Si|CoO_x (green curves) and n-Si|$NiCoO_x$ (blue curves) in contact with ACS grade 1.0 M KOH(aq). The open-circuit photovoltage, V_{oc}, short-circuit photocurrent density, J_{sc}, and fill factor, *ff*, of a

photodiode that would produce the same shift in *J-E* behavior as that observed for the n-Si photoanodes relative to p$^+$-Si dark anodes, both coated with nominally the same film in each case, was extracted from a load-line analysis (see Supporting Information) on the *J-E* behavior of n-Si electrodes relative to the p$^+$-Si electrodes (Table 1). As expected from the transmittance and reflectance characteristics (Figures 3,5), CoO$_x$ films produced the lowest J_{sc} values and NiO$_x$ produced the highest J_{sc} values. The open-circuit voltage showed relatively little variation between coatings. The fill factors reflected a trade-off between decreasing J_{sc} values and increasing $\eta_{10 \text{ mA cm-2}}$ as the film composition was changed from NiO$_x$ to NiCoO$_x$ and then to CoO$_x$, with NiCo$_x$ having the lowest fill factor due to the co-variation in these performance characteristics resulting from changes in the film composition. Despite the reductions in J_{sc} and changes in *ff*, the ideal regenerative cell photoelectrode efficiencies, η_{IRC},[24] varied relatively little as the film composition was changed.

Impedance measurements on n-Si|NiO$_x$, n-Si|CoO$_x$ and n-Si|NiCoO$_x$ electrodes analyzed with an equivalent circuit consisting of a resistor in series with a parallel combination of a resistor and capacitor yielded good fits to semicircles in Nyquist plots. Mott-Schottky analysis (Figure S7) of the impedance behavior of coated n-Si electrodes in contact with 50 mM Fe(CN)$_6^{3-}$ and 350 mM Fe(CN)$_6^{4-}$ in 1.0 M Na$_2$SO$_4$(aq) in the dark yielded a flat-band potential, V_{fb} vs the Nernstian potential of the Fe(CN)$_6^{3-/4-}$ solution of -0.519 ± 0.002 for NiO$_x$, -0.552 ± 0.005 for CoO$_x$, and -0.528 ± 0.003 V for NiCoO$_x$ films, respectively. The flat-band data are consistent with the slightly higher V_{oc} observed for CoO$_x$-coated electrodes relative to n-Si|NiO$_x$ or n-Si|NiCoO$_x$ electrodes (Table 1).

Figure S8 depicts the Faradaic efficiency for production of $O_2(g)$ by n-Si|NiO$_x$, n-Si|CoO$_x$ and n-Si|NiCoO$_x$ photoelectrodes in contact with ACS grade 1.0 M KOH(aq) under simulated AM1.5 illumination. A current density of $\sim$ 8 mA cm^{-2} produced a potential of $\sim$ 1.8 V versus RHE for these activated electrodes, with illumination maintained for 24 h. The mass of O_2 expected from the total photogenerated charge passed, assuming 100% faradic efficiency, was in excellent agreement with the mass of O_2 observed by water displacement.

Figure 6 presents the photoelectrochemical behavior of n-Si|NiO$_x$, n-Si|CoO$_x$ and n-Si|NiCoO$_x$ photoanodes in contact with ACS grade 1.0 M KOH(aq) under simulated AM1.5 illumination. Figure 6a, 6b and 6c display the *J-E* data collected during the stability evalution on n-Si|NiO$_x$, n-Si|CoO$_x$ and n-Si|NiCoO$_x$ respectively, after 0, 200 or 400 h of continuous operation. Figure 6a shows that the NiO$_x$-coated photoanode degraded after 400 h of continuous operation at 1.75 V vs. RHE, exhibiting a distinct decrease in *ff*. During this time period, the light-limited current density decreased by 21.2%, from 28.7 to 22.6 mA cm^{-2}. SEM data (inset) indicated the formation of 2-5 μm diameter pinholes. This behavior is consistent with the conversion, during the electrochemical measurements, of NiO$_x$ to structurally porous Ni(OH)$_2$/NiOOH, which partially exposes the Si photoanode surface to the corrosive KOH solution. In contrast, CoO$_x$-coated n-Si photoanodes were quite stable even after 400 h of continuous operation under 1.75 V vs. RHE bias in ACS grade 1.0 M KOH(aq) (Figure 6b). The light-limited current density actually increased by 21.3%, from 19.2 to 23.3 mA cm^{-2}, after 400 h of continuous operation. SEM data (inset) showed the formation of 10-50 μm diameter pinholes, but the dissolution and re-organization of the film enabled more light to pass

through and hence increased the photocurrent density. After 400 h of continuous operation under 1.75 V vs. RHE bias in ACS grade 1.0 M KOH(aq), $NiCoO_x$-coated n-Si photoanodes exhibited a moderate decrease in *ff* (Figure 6c). The light-limited current density increased by 9.8%, from 23.5 to 25.8 mA cm^{-2}, after 60 h continuous operation, which is consistent with dissolution of CoO_x. The light-limited current density decreased from 25.8 to 20.1 mA cm^{-2} at the end of 400 h continuous operation, corresponding to a 14.4% decrease from its initial value (Figure 6d). The conversion of NiO_x to structurally porous $Ni(OH)_2$/NiOOH during the stability test dominated the performance of $NiCoO_x$ electrodes, eventually leading to a slow decrease of the photocurrent at 1.75 V vs RHE. The SEM data (inset) indicated the formation of 5-20 μm diameter pinholes, which is between the pinhole size generated in NiO_x and CoO_x films.

Figure S9 displays XPS survey scans of the 75 nm-thick TCO-coated n-Si|$NiCoO_x$ photoanodes before and after, respectively, 400 h of continuous operation under AM1.5 illumination in ACS grade 1.0 M KOH(aq). Signals in both the Ni 2p region and Co 2p region diminished substantially after the 400 h stability test, whereas trace impurities were absorbed from the solution. Detailed examination indicated the presence of trace amounts of Fe, Ag, Cu, N, Ca, As and Cl on the electrode surface, either from the solution or from the glassware used in the stability test experiment.

The comparison performed herein indicates that the increased optical absorption resulting from partial substitution of Co for Ni decreases the photocurrent density and thus deleteriously affects the efficiency of planar Si photoanodes coated uniformly with these TCO films. The results also suggest, however, that Co-containing TCO's could be advantageously exploited as multi-functional protection layers in conjunction with

strategies that minimize optical absorption losses on photoelectrodes, such as formation of microcone arrays,[25] dispersion of the catalyst into nanometer-sized islands onto the electrode surface,[26, 27] or similar approaches that minimize the effects of absorption and reflection losses in the catalyst while maintaining the beneficial effects of p-type TCO films that can enhance the stability of the coated photoanode in the catalyst-coated regions of the Si light absorber.

The thickness of p-TCOs analyzed in this work was kept consistent to compare the effect of film composition on OER activity and stability. Increased photocurrents could be obtained at Si photoanodes coated with thinner p-TCO films containing Co without a significant reduction in OER activity. The interface between the p-TCOs and Si was not optimized in this work, due to the damage caused by the high-energy ions during sputtering. Moreover, sputtered p-TCO films only provide enhanced photoelectrode performance on planar, self-passivating semiconductor surfaces, due to the directional film growth of sputtering as well as the formation of defects and pinholes during film growth. Alternative methods, such as atomic-layer deposition (ALD), may improve the interfacial energetics and enable film deposition on high-aspect ratio, nanostructured surfaces and other surfaces and morphologies where such approaches can provide enhanced stability as well as catalytic activity in conjunction with favorable anti-reflection coating properties. Silicon photoanodes could be a potential component of a tandem light-absorber structure for a complete integrated solar-fuels device, and also provide a proof-of-concept of the implementation of the TCO-coating approach for a variety of photoelectrode materials and systems.

CONCLUSIONS

NiO$_x$, CoO$_x$ and NiCoO$_x$ films prepared using RF reactive sputtering are intrinsically p-type, optically transparent, electrically conductive oxides that form a heterojunction with Si that enables hole conduction. All of the films acted not only as a protection layer but also were active catalysts for the oxygen-evolution reaction in aqueous alkaline media. The films yielded relatively stable photoanodes for production of O$_2$(g) in 1.0 M KOH(aq) for 400 h under simulated AM1.5 illumination. Collectively this family of materials offers the ability to tune the porosity, optical absorption and catalytic properties to obtain optimized protection layers for a variety of distinct photoanode morphologies, optimizing light management while minimizing exposure of the absorber to the corrosive electrolyte.

ASSOCIATED CONTENT

Detailed electrode preparation, XPS analysis, EIS and Mott-Schottky analysis, Photoelectrochemical measurements and Load-line analysis can be found in the supplementary information.

ACKNOWLEDGMENTS

Center (MMRC) in the Beckman Institute at the California Institute of Technology. Paul

Kempler and Weilai Yu are thanked for assistance with editing the manuscript.

REFERENCES

1.   N. S. Lewis and D. G. Nocera, *Proceedings of the National Academy of Sciences*,
        2006, **103**, 15729-15735.

2.   M. G. Walter, E. L. Warren, J. R. McKone, S. W. Boettcher, Q. Mi, E. A. Santori
        and N. S. Lewis, *Chemical Reviews*, 2010, **110**, 6446-6473.

3.   Y. Lee, J. Suntivich, K. J. May, E. E. Perry and Y. Shao-Horn, *The Journal of
        Physical Chemistry Letters*, 2012, **3**, 399-404.

4.   E. A. Paoli, F. Masini, R. Frydendal, D. Deiana, C. Schlaup, M. Malizia, T. W.
        Hansen, S. Horch, I. E. L. Stephens and I. Chorkendorff, *Chemical Science*, 2015,
        6, 190-196.

5.   B. Mei, B. Seger, T. Pedersen, M. Malizia, O. Hansen, I. Chorkendorff and P. C.
        K. Vesborg, *The Journal of Physical Chemistry Letters*, 2014, **5**, 1948-1952.

6.   K. Sun, N. Park, Z. Sun, J. Zhou, J. Wang, X. Pang, S. Shen, S. Y. Noh, Y. Jing,
        S. Jin, P. K. L. Yu and D. Wang, *Energy & Environmental Science*, 2012, **5**,
        7872-7877.

7.   M. J. Kenney, M. Gong, Y. Li, J. Z. Wu, J. Feng, M. Lanza and H. Dai, *Science*,
        2013, **342**, 836-840.

8.   K. Sun, S. Shen, J. S. Cheung, X. Pang, N. Park, J. Zhou, Y. Hu, Z. Sun, S. Y.
        Noh, C. T. Riley, P. K. L. Yu, S. Jin and D. Wang, *Physical Chemistry Chemical
   Physics*, 2014, **16**, 4612-4625.

9.   K. Sun, M. T. McDowell, A. C. Nielander, S. Hu, M. R. Shaner, F. Yang, B. S. Brunschwig and N. S. Lewis, *The Journal of Physical Chemistry Letters*, 2015, **6**, 592-598.

10.   L. Trotochaud, S. L. Young, J. K. Ranney and S. W. Boettcher, *Journal of the American Chemical Society*, 2014, **136**, 6744-6753.

11.   D. Singh, *Journal of The Electrochemical Society*, 1998, **145**, 116-120.

12.   K. V. Rao and A. Smakula, *Journal of Applied Physics*, 1965, **36**, 2031-2038.

13.   F. Lin and S. W. Boettcher, *Nature Materials*, 2014, **13**, 81-86.

14.   I. M. Sadiek, A. M. Mohammad, M. E. El-Shakre, M. I. Awad, M. S. El-Deab and B. E. El-Anadouli, *Int. J. Electrochem. Sci.*, 2012, **7**, 3350-3361.

15.   C. C. L. McCrory, S. Jung, J. C. Peters and T. F. Jaramillo, *Journal of the American Chemical Society*, 2013, **135**, 16977-16987.

16.   J. Yang, K. Walczak, E. Anzenberg, F. M. Toma, G. Yuan, J. Beeman, A. Schwartzberg, Y. Lin, M. Hettick, A. Javey, J. W. Ager, J. Yano, H. Frei and I. D. Sharp, *Journal of the American Chemical Society*, 2014, **136**, 6191-6194.

17.   X. Zhou, R. Liu, K. Sun, D. Friedrich, M. T. McDowell, F. Yang, S. T. Omelchenko, F. H. Saadi, A. C. Nielander, S. Yalamanchili, K. M. Papadantonakis, B. S. Brunschwig and N. S. Lewis, *Energy & Environmental Science*, 2015, **8**, 2644-2649.

18.   R. R. Owings, G. J. Exarhos, C. F. Windisch, P. H. Holloway and J. G. Wen, *Thin Solid Films*, 2005, **483**, 175-184.

19.   Y. Yang, H. Fei, G. Ruan, C. Xiang and J. M. Tour, *ACS Nano*, 2014, **8**, 9518-9523.

20.   L. Chen, J. Yang, S. Klaus, L. J. Lee, R. Woods-Robinson, J. Ma, Y. Lum, J. K. Cooper, F. M. Toma, L.-W. Wang, I. D. Sharp, A. T. Bell and J. W. Ager, *Journal of the American Chemical Society*, 2015, **137**, 9595-9603.

21.   D. Bae, B. Mei, R. Frydendal, T. Pedersen, B. Seger, O. Hansen, P. C. K. Vesborg and I. Chorkendorff, *ChemElectroChem*, 2016, DOI: 10.1002/celc.201500554.

22.   S. Hu, M. R. Shaner, J. A. Beardslee, M. Lichterman, B. S. Brunschwig and N. S. Lewis, *Science*, 2014, **344**, 1005-1009.

23.   M. S. Burke, M. G. Kast, L. Trotochaud, A. M. Smith and S. W. Boettcher, *Journal of the American Chemical Society*, 2015, **137**, 3638-3648.

24.   R. H. Coridan, A. C. Nielander, S. A. Francis, M. T. McDowell, V. Dix, S. M. Chatman and N. S. Lewis, *Energy & Environmental Science*, 2015, **8**, 2886-2901.

25.   S. Yalamanchili, E. Verlage, W.-H. Cheng, K. T. Fountaine, P. R. Jahelka, P. A. Kempler, R. Saive, N. S. Lewis and H. A. Atwater, *Nano Letters*, 2020, **20**, 502-508.

26.   K. Sun, Nicole L. Ritzert, J. John, H. Tan, W. G. Hale, J. Jiang, I. Moreno-Hernandez, K. M. Papadantonakis, T. P. Moffat, B. S. Brunschwig and N. S. Lewis, *Sustainable Energy & Fuels*, 2018, **2**, 983-998.

27.   P. A. Kempler, H. J. Fu, Z. P. Ifkovits, K. M. Papadantonakis and N. S. Lewis, *The Journal of Physical Chemistry Letters*, 2019, **11**, 14-20.

Table 1. Properties of NiO_x, $NiCoO_x$, and CoO_x

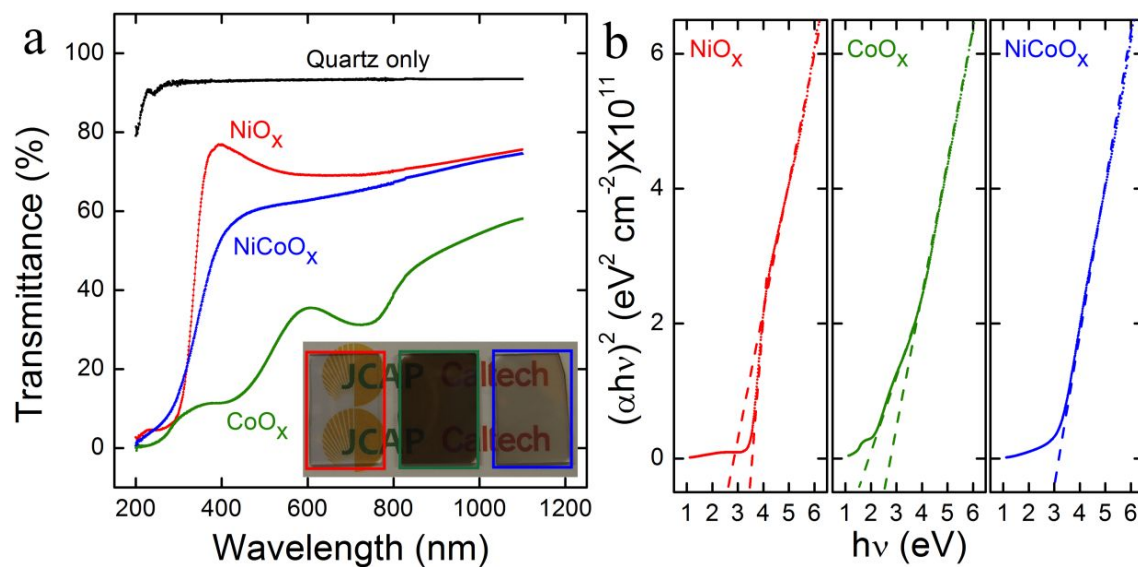|	**NiO_x**	**$NiCoO_x$**	**CoO_x**
Surface Roughness, nm	4.08 ± 0.03	3.33 ± 0.07	4.24 ± 0.15
Transmittance (390-1100 nm),%	70	60	30
Band Gap, eV	2.6 (i), 3.5(d)	3.0(d)	1.6 (d), 2.5(d)
$\eta_{10 \text{ mA cm}}$-2 (ACS KOH), mV	330 ± 5	357 ± 5	420 ± 10
$\eta_{10 \text{ mA cm-2}}$ (FCC KOH), mV	600 ± 5	390 ± 5	440 ± 8
V_{oc}, mV	250 ± 15	270 ± 10	290 ± 10
$J_{sc,}$ mA cm^{-2}	28 ± 0.3	24 ± 0.5	18 ± 0.3
ff	0.35	0.33	0.39
η_{IRC}, %	2.40	2.14	2.05
$V_{fb,}$ V vs Fe(CN)$_6{}^{3-/4-}$	-0.519 ± 0.002	-0.528 ± 0.003	-0.552 ± 0.005
$J_{ph}(0)$, mA cm^{-2}	28.7	23.5	19.2
$J_{ph}(400 \text{ h})$, mA cm^{-2}	22.6	20.1	23.3

FIGURES
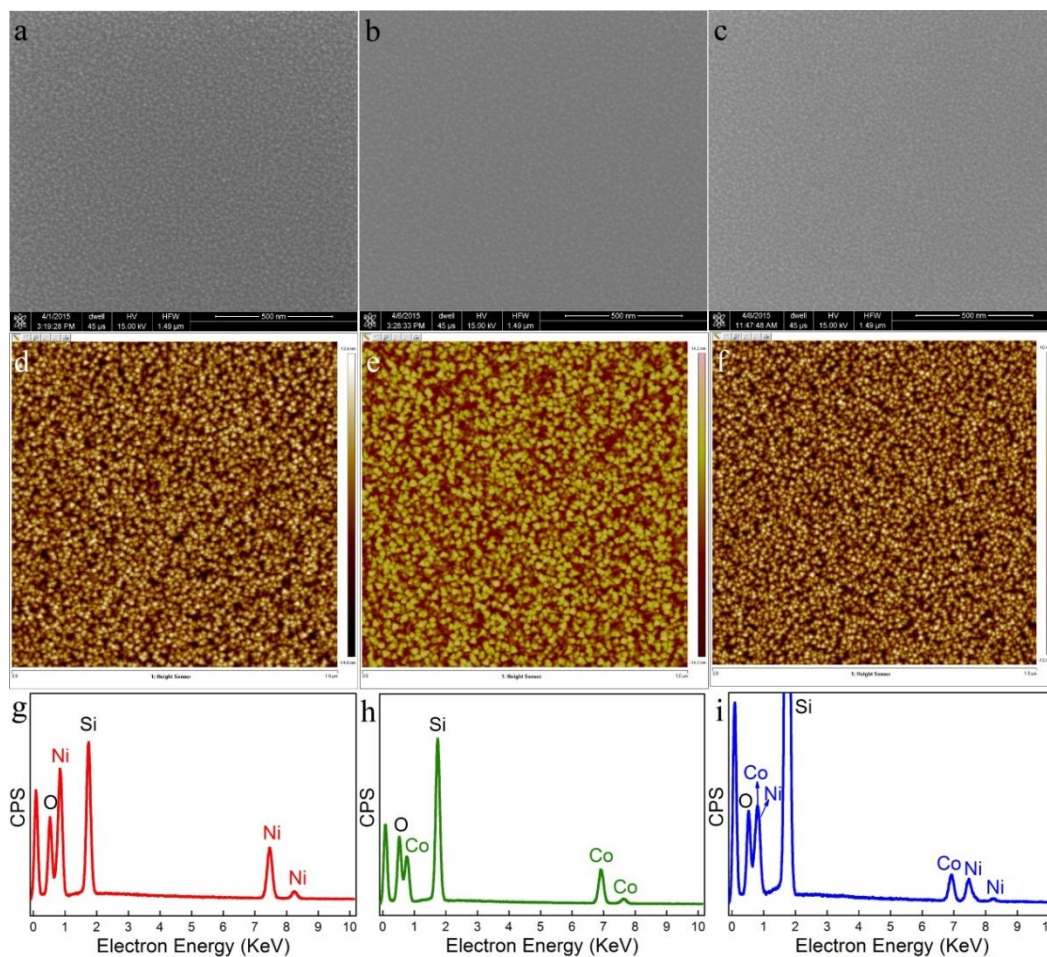
Figure 1. SEM images of 75 nm thick (a) NiO_x, (b) CoO_x and (c) $NiCoO_x$ on a p^+-Si substrate. AFM images of 75 nm thick (d) NiO_x, (e) CoO_x and (f) $NiCoO_x$ on P^+-Si substrate. EDS data of (g) 360 nm NiO_x, (h) 300 nm CoO_x and (i) 150 nm $NiCoO_x$ on a p^+-Si substrate.
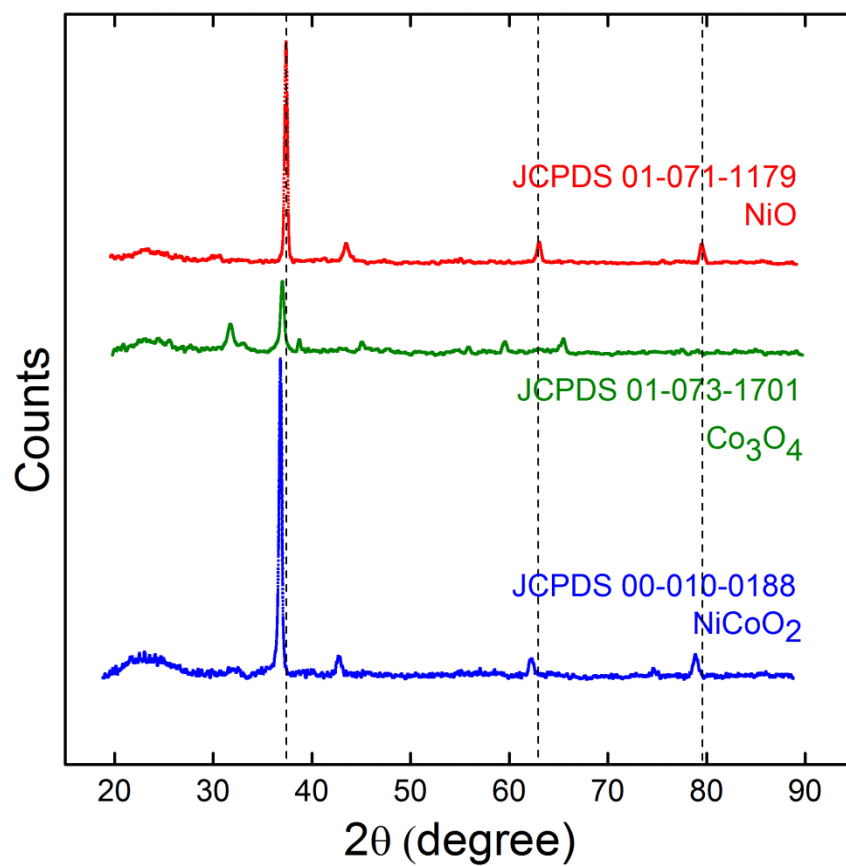
Figure 2. XRD pattern of NiO_x(red curve), CoO_x(green curve) and $NiCoO_x$(blue curve) films sputtered on glass substrate.

Figure 3. (a) Transmittance of 75 nm NiO_x (red curve), CoO_x (green curve) and $NiCoO_x$ (blue curve) and bare quartz (black curve). Inset shows a digital image of 75 nm NiO_x, CoO_x and $NiCoO_x$ coated on quartz substrate. (b) Tauc plots ($h\nu$ versus $(\alpha h\nu)^2$) for 75 nm NiO_x (red curve), CoO_x (green curve) and $NiCoO_x$ (blue curve).
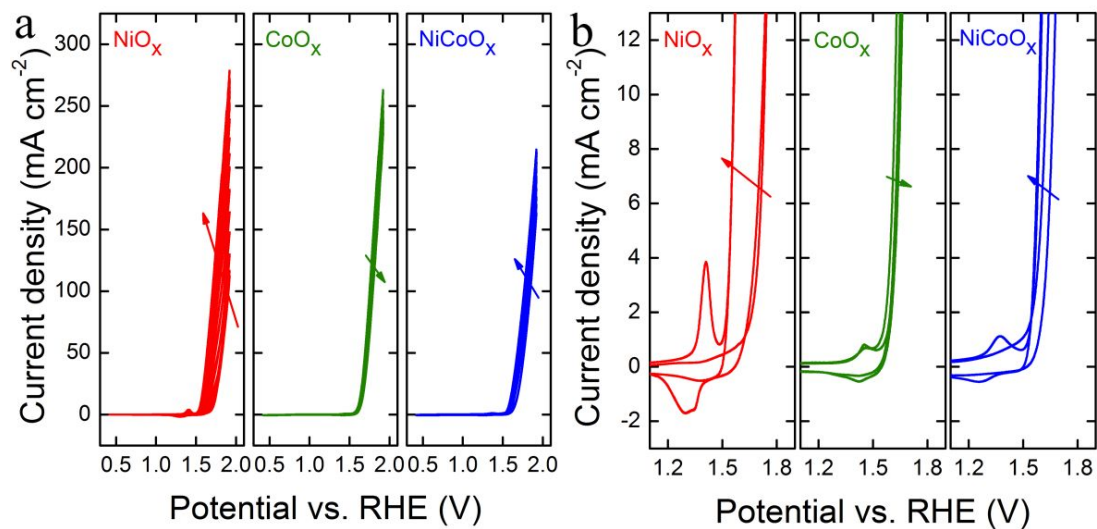
Figure 4. (a) 20 cyclic voltammetric sweeps of p$^+$-Si|NiO$_x$ (red curve), p$^+$-Si|CoO$_x$ (green curve)and p$^+$-Si|NiCoO$_x$ (blue curve) in 1.0 M KOH(aq, ACS grade), showing the activation and dark catalytic activity of all the sputtered films. (b) Expansion of (a) with only the first and 20th scans shown.
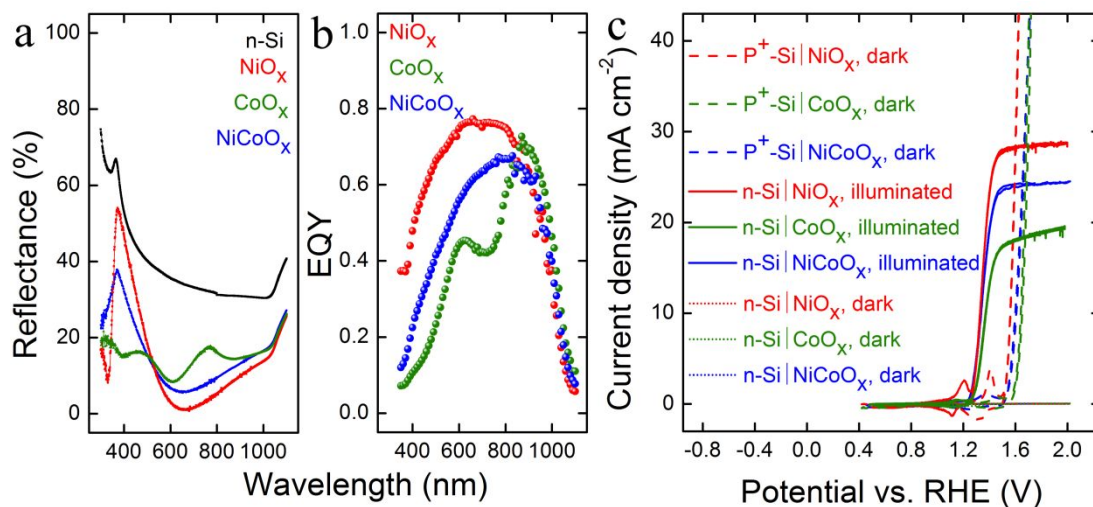
Figure 5. (a) Reflectance spectra of 75 nm-thick NiO_x (red curve), CoO_x (green curve) and $NiCoO_x$ (blue curve) on n-Si, as well as a freshly etched n-Si substrate (black curve). (b) External quantum yield (Φ_{ext}) of 75 nm-thick NiO_x (red curve), CoO_x (green curve) and $NiCoO_x$ (blue curve) on n-Si measured in 1.0 M KOH(aq, ACS grade) at 1.75 V versus RHE. (c) *J-E* behavior (at a scan rate of 50 mV s^{-1}) of n-Si|NiO_x (solid red curve), n-Si|CoO_x (solid green curve) and n-Si|$NiCoO_x$ (solid blue curve) under simulated AM1.5 illumination and n-Si|NiO_x (dotted red curve), n-Si|CoO_x (dotted green curve) and n-Si|$NiCoO_x$ (dotted blue curve) in the dark in contact with 1.0 M KOH(aq, ACS grade).
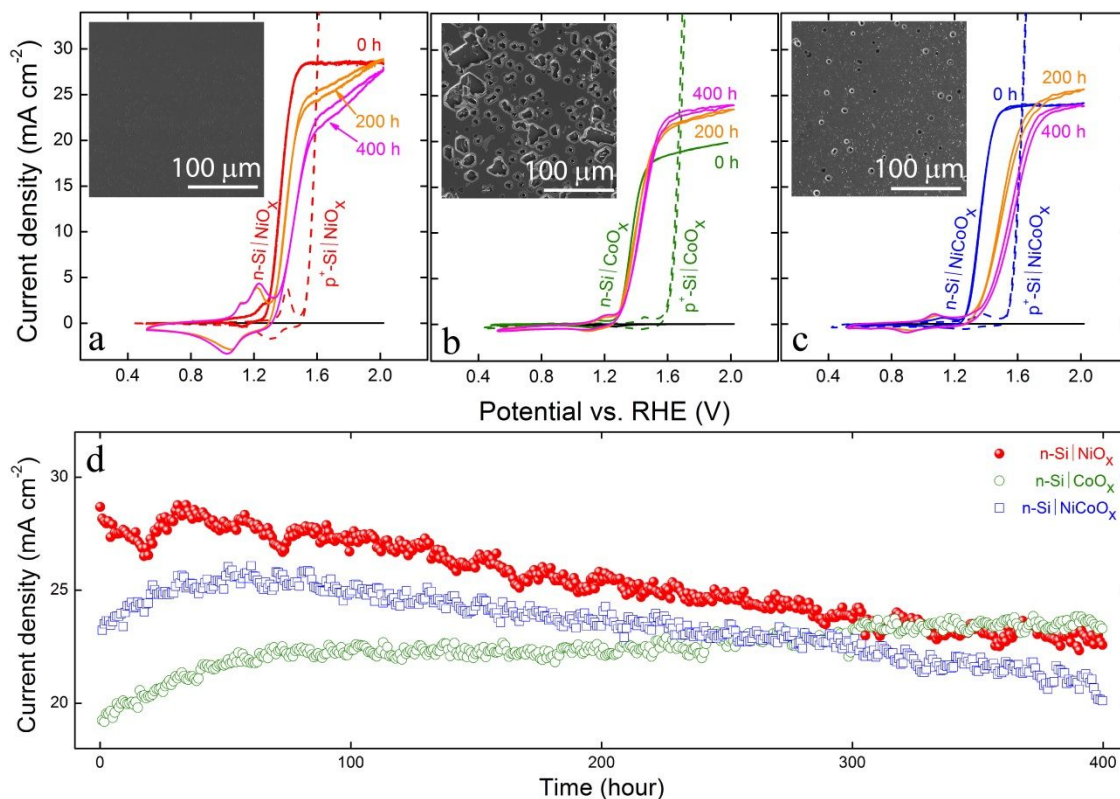
Figure 6. *J-E* data collected before, during and after a 400-h chronopotentiometric stability test on (a) n-Si|NiO$_x$, (b) n-Si|CoO$_x$ and (c) n-Si|NiCoO$_x$ photoanodes under AM1.5 illumination in 1.0 M KOH (aq, ACS grade). Inset shows the SEM images (with a scale bar of 100 μm) of surface damage on n-Si electrodes after 400 h of stability testing. (d) Chronoamperometry of n-Si|NiO$_x$ (red solid dot), n-Si|CoO$_x$ (green hollow dot) and n-Si|NiCoO$_x$ (blue hollow square) for 400 h in 1.0 M KOH (aq, ACS grade) under AM1.5 illumination, with electrode potential was held at 1.75 V versus RHE, and the electrochemical cell under air flow cooling (to prevent heating of the electrode and solution).
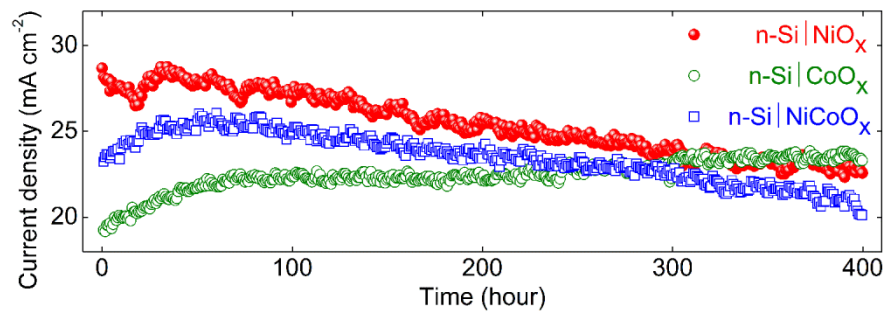
Table of Contents